True 2D-to-3D Reconstruction of Heterogeneous Porous Media via Deep Generative Adversarial Networks (GANs)

Hamed Amiri[1], Hannah Vogel[1], and Oliver Plümper[1]

[1]Utrecht University

March 05, 2024

True 2D-to-3D Reconstruction of Heterogeneous Porous Media via Deep Generative Adversarial Networks (GANs)

Hamed Amiri[1*], Hannah Vogel[1†], Dr. Oliver Plümper[1]

[1]Department of Earth Sciences, Faculty of Geoscience, Utrecht University, Utrecht, The Netherlands

Key Points:

- Rapid and reliable 3D reconstructions of porous media using generative adversarial networks (GANs)
- A new workflow is proposed for 3D image reconstruction of porous media using purely 2D electron and optical microscopy images.
- Our model can generate realistic 3D images with high variability to assess the uncertainty of heterogeneous rocks

*Co-first author
†Co-first author

Corresponding author: Hamed Amiri, `h.amiri@uu.nl`

Abstract

Accurately characterizing rock microstructures in three dimensions (3D) is crucial for modeling various physical phenomena and estimating rock properties. Despite advancements in 3D imaging, limitations arise from the trade-off between sample size and resolution, particularly in heterogeneous rocks with multi-scale features where both high resolution and a large field of view (FOV) are essential. These challenges have prompted interest in accurate 3D reconstructions from high-resolution two-dimensional (2D) images using advanced generative models like generative adversarial networks (GANs). In this study, using scanning electron microscopy (SEM) and optical microscopy, we acquired 2D images from three orthogonal sections of a Berea sandstone sample. These images were employed to train a modified SliceGAN model, a variant of GANs, for 3D reconstruction. Unlike previous studies utilizing SliceGAN or similar methods for 2D-to-3D reconstructions that incorporated 3D images in their training, our approach is unique in that it relies exclusively on 2D images. Our results show that the proposed workflow and modifications in the architecture and training of SliceGAN enable us to produce 3D reconstructions that closely mirror real 3D X-ray tomography in terms of structural and morphological characteristics. Additionally, we highlight our model's ability to generate diverse reconstructions with transport properties that align with previous studies on Berea sandstone. This underscores the potential of 2D-to-3D reconstructions as an effective alternative to multiple X-ray tomographies, integral for assessing variability in heterogeneous rocks.

Plain Language Summary

Describing rock microstructures in 3D is crucial for modeling rock properties, such as permeability, and physical transport processes, like fluid flow through a rock. One method to estimate such rock properties is digital rock physics which involves first imaging and digitizing the microstructures and then numerically simulating different physical processes. To capture both fine-scale features and overall variability within a sample, detailed images alongside large sample areas are necessary. However, 3D imaging techniques like X-ray tomography struggle with a trade-off between sample size and image resolution. 2D imaging techniques, like electron and optical microscopy, offer a solution providing large fields of view and high-resolution images. New ways of creating realistic 3D rock volumes have recently emerged using deep learning-based generative models such as Generative Adversarial Networks (GANs). We employ a variant of GANs to train on purely 2D images, rapidly generating realistic 3D volumes of Berea sandstone. Our analysis shows that the adjusted model can generate diverse 3D reconstructions displaying properties consistent with established knowledge of Berea sandstone. Our findings highlight the usefulness of true-2D-to-3D rock reconstructions as a rapid and reliable means of generating large and diverse sample pools for assessing complex rock properties.

1 Introduction

The macroscopic transport properties and physical processes of porous media are intricately governed by their three-dimensional (3D) microstructure. Therefore, achieving an accurate characterization of microstructures is paramount for estimating desired properties and simulating diverse physical phenomena (Al-Raoush & Willson, 2005; Blunt et al., 2013; Bakke & Øren, 1997). Key properties such as porosity, pore size distribution, pore connectivity, and permeability play a pivotal role in the reliable modeling of transport-related phenomena (Bear, 2013; Blunt, 2017; Singh et al., 2017; Sahimi, 2011). These properties are crucial for understanding and simulating processes such as groundwater transport (Bear, 2010), storage of CO_2 (Krevor et al., 2015; Tang et al., 2021) and hydrogen (Heinemann et al., 2021), geothermal energy utilization (K.-Q. Li et al., 2020;

Lichtner & Karra, 2014), and reservoir characterization (Wu, Tahmasebi, Lin, Zahid, et al., 2019; Blunt & Lin, 2022; C. F. Berg et al., 2017).

Recent technological strides in imaging techniques, including non-destructive X-ray (micro)-Computed Tomography (μCT) (Blunt et al., 2013) and focused ion beam scanning electron microscope (FIB-SEM) (Hemes et al., 2015), have empowered researchers with robust tools to capture intricate representations of complex microstructures. The enhancement in hardware capabilities, coupled with the ever-increasing computational power and ongoing improvements in model complexity and efficiency, has facilitated the generation of increasingly realistic 3D models of porous media (Liu et al., 2019; Wildenschild & Sheppard, 2013; Cnudde & Boone, 2013).

Despite remarkable technological advances, a persistent challenge in imaging porous media is the inherent trade-off between image resolution and sample size. High-resolution images are often acquired by scanning smaller samples, which may not be representative of the entire rock. This compromise introduces a dilemma: opting for high resolution may result in localized observations that fail to capture the overall heterogeneity, long-range patterns, and variability present in natural samples. On the other hand, scanning larger samples for a more holistic representation leads to a lower resolution, potentially limiting the ability to resolve finer-scale features. An extra layer of complexity may be added in heterogeneous media such as carbonates (Dehghan Khalili et al., 2013; Menke et al., 2018) and shales (Wu, Tahmasebi, Lin, Ren, & Dong, 2019), where a hierarchical microstructure at varying length scales is often present, necessitating the use and integration of different imaging techniques (Brandon & Kaplan, 2013; X.-Y. Yang et al., 2017). In addition, due to randomness and stochasticity present in natural samples, several realizations are required to evaluate variability and provide an uncertainty estimation of the rock properties. Furthermore, 3D imaging techniques are time-consuming and rely on highly specialized equipment, which can be expensive and not always readily accessible (Valsecchi et al., 2020; Bodla et al., 2014; Wu et al., 2018; Hajizadeh et al., 2011).

In comparison, two-dimensional (2D) imaging techniques, such as scanning electron microscopy (SEM) and especially optical light microscopy, offer several significant advantages, including higher achievable resolutions, larger fields of view (FoV), rapid scanning speeds, and often reduced associated costs. Leveraging their high-resolution imaging capabilities, 2D imaging techniques excel in the detection of intricate features at the micron to sub-micron scale across more expansive and consequently more representative areas. This proficiency makes 2D methods a viable alternative to 3D imaging techniques in effectively capturing both essential fine-scale features and the inherent heterogeneity within the sample (Fu et al., 2022; Dahari et al., 2023). Moreover, 2D images are more easily obtained and can be promptly utilized to quantify statistical spatial morphologies and microstructural characteristics (e.g., porosity, specific surface area, and pore sizes) within porous media (Torquato & Stell, 1982; Torquato & Haslach Jr, 2002). Nonetheless, a conspicuous limitation persists – 2D images can only provide 2D information about heterogeneous pore microstructures. This limitation proves problematic since various material behaviors, such as fluid flow, are intrinsically volumetric in nature (Gayon-Lombardo et al., 2020).

Addressing this, 3D reconstruction of heterogeneous media via high-resolution 2D images has become an active research area in digital rock physics. The 2D-to-3D image reconstruction is an inverse problem in which limited microstructural data (e.g., 2D images) are used to generate statistically equivalent microstructures with larger sizes and/or additional dimensions. This provides representative 3D microstructural information at resolutions sufficient for detecting multi-scale features within the samples (Jiao et al., 2007; Yeong & Torquato, 1998; Amiri et al., 2023; Sahimi & Tahmasebi, 2021).

Currently, the methods proposed for these 2D-to-3D reconstructions can be largely grouped into two categories: stochastic and deep learning-based methods. The stochastic methods are mainly founded on microstructure characterization and approach the reconstruction as an optimization problem. The characterization entails the initial imaging of material followed by statistical quantification of microstructures using spatial correlation functions, also recognized as statistical microstructure descriptors (SMDs) (Bostanabad et al., 2018). These SMDs then serve as target functions in an optimization technique, most commonly simulated annealing, to generate 3D microstructures whose SMDs align closely with those observed in the original 2D images, thereby ensuring a faithful representation of the material's inherent characteristics. The most common and basic SMD is the two-point correlation function (S_2) that has been used successfully for 3D reconstruction (Jiao et al., 2007, 2008; Sheehan & Torquato, 2001; Karsanina & Gerke, 2018).

However, the statistical information captured by S_2 alone is not sufficient in the case of heterogeneous microstructures with complex structure and morphology (Jiao et al., 2010; Gommes et al., 2012; Amiri et al., 2023). To overcome the limitations, other studies (Hajizadeh et al., 2011; Tahmasebi & Sahimi, 2012) have turned to high-order n-point correlation functions ($n \geq 3$) to more precisely quantify higher-order spatial patterns in complex microstructures, thus enhancing reconstruction accuracy. However, the computation of these n-point correlations and their specific subsets, termed n-point polytope functions (Chen et al., 2019), incurs significant computational costs. Moreover, the process of generating microstructures is notably slow, and the resulting microstructures lack diversity. The latter is because all generated structures are required to match the real ones in terms of the target functions (i.e., SMDs). This limitation restricts the method's ability to provide insights into the variability of rock properties.

In recent years, the realm of deep learning (DL), especially deep generative models, has witnessed remarkable progress, becoming key in overcoming the limitations of stochastic methods. The core aim of these models is to grasp the underlying probability distribution of a dataset by drawing samples from it (i.e., training dataset), aiming to generate new samples with the same distribution. Training these models typically involves sampling from a simple, known (prior) distribution like the Gaussian distribution. The model is then trained to map this prior distribution to that of the training data, often using a deep neural network (I. Goodfellow, 2016; Bond-Taylor et al., 2021). Among various generative models used in microstructure reconstruction, variational autoencoders (VAEs) (Kingma & Welling, 2013; Shams et al., 2020; Laloy et al., 2017), normalizing flows (NFs) (Kingma & Dhariwal, 2018; Guan et al., 2021), and GANs (You et al., 2021; Liu et al., 2019; J. Li et al., 2023; Feng et al., 2019; T. Zhang et al., 2023; Y. Yang et al., 2022) are the most prevalent. Here, we particularly focus on studies pertaining to 2D-to-3D reconstruction using GANs. For more details on microstructure reconstruction using other methods, the reader can refer to the comprehensive review by Mirzaee et al. (2023).

GANs have garnered considerable attention in research, primarily for their success in generating high-quality images. Opposed to VAEs and NFs, which are explicit generative models, GANs are implicit models that do not explicitly estimate the data distribution but learn to generate data in an adversarial training process. This process involves two neural networks competing against each other to improve the realism and details of generated images without the constraints of likelihood computation that are inherent in VAEs and NFs. Furthermore, GANs's generator has fewer limitations compared to other methods, enhancing its versatility and adaptability for diverse applications and integration with other generative models (I. Goodfellow, 2016; Bond-Taylor et al., 2021).

Due to the above-mentioned attractions of 2D images and the advantages of GANs, several studies have tried to reconstruct 3D microstructures using 2D images. Volkhonskiy et al. (2019) used a hybrid VAE-GAN in which a conditional GAN (cGAN) was combined with an encoder to reconstruct 3D images from 2D slices. The encoder learns to map the slices of a 3D image into a latent space which then feeds with noise (i.e., samples from random normal distribution) into a 3D generator. In another hybrid method, Feng et al. (2020) redesigned BicycleGAN (Zhu et al., 2017), initially introduced for 2D to 2D image translation, by combining it with an encoder in an end-to-end framework. Their results show that, given a target 3D image, their model can reconstruct statistically equivalent 3D images with similar characteristics. You et al. (2021) performed the 2D to 3D reconstruction via interpolation in latent space of progressive growing GAN (PG-GAN)(Karras et al., 2017). The latent space refers to a lower dimensional space in which there exists a compact representation of the generated data called latent code. However, since GANs are not invertible by default, it takes a further step of optimization or training an encoder to obtain the latent vectors corresponding to generated images by GAN, a process known as GAN inversion (Xia et al., 2021). In this work, a PG-GAN was first trained with 2D grayscale images of carbonate slices of a 3D image. Then, the latent codes corresponding to sparse slices along one axis were obtained through a gradient descent optimization. Finally, by interpolation between sparse latent codes and feeding them to the trained generator, a 3D image was reconstructed.

Another novel 2D-to-3D reconstruction method, called SliceGAN, was demonstrated by Kench and Cooper (2021). In this method, a 3D generator is trained against three 2D discriminators, each for a distinct axis. During the training, the generated 3D images are sliced and along with real slices of the same orientations are fed into the respective discriminators, ensuring that the synthesized 3D image closely resembles 2D images in each orientation. Inspired by StyleGAN (Karras et al., 2019), Chung and Ye (2021) further adapted this method by incorporating adaptive instance normalization (AdaIN) for better attribute control on the generated images. Other studies, such as Sciazko et al. (2021) and Valsecchi et al. (2020), applied similar methodologies with a single 2D discriminator, which is particularly suitable for isotropic systems. While showing promising results, these studies still rely on 3D volumes and /or the slices taken from a 3D volume during the training, making them pseudo-2D-to-3D reconstruction methods.

In this study, we design a novel workflow for true 2D-to-3D reconstruction. We adapt the sampling process in the original SliceGAN to enable the reconstruction of 3D images exclusively from 2D inputs. Additionally, we propose an efficient performance metric for the model based on the correlation functions in 2D and 3D. As training data, we specifically utilize 2D SEM and optical images obtained from three orthogonal thin sections of Berea Sandstone. Scanned at different pixel sizes (3.8 μm for SEM and 0.44 μm for optical images), these 2D images cover a large area of sample faces. This allows us to capture a broader range of heterogeneities in the training images and therefore in the 3D reconstructions. To validate our reconstructions, we compare them with a 3D X-ray tomography of the same sample, as well as previously reported results on the transport properties of Berea sandstone. Our findings show that 3D reconstructions from representative 2D images not only resemble the actual sample in terms of visual and quantitative measures but also provide valuable insights into the variability of rock properties. The ability to generate diverse microstructure is particularly significant, indicating that rather than performing multiple, costly, and time-consuming X-ray tomographies, we can employ 2D images to reconstruct numerous 3D realizations for quantifying the uncertainty of rock properties.

2 Methods

The goal of the present work is to propose a workflow for 3D microstructure reconstruction using 2D images. Specifically, we modify SliceGAN and investigate its accuracy in synthesizing realistic volumes of Berea sandstone. Our model is trained exclusively on representative 2D binary images derived from two distinct 2D imaging techniques: SEM and optical light microscopy. For validation purposes, a μCT image of the same sample is acquired but is used to verify the accuracy of our model, not for its training. To conduct a comprehensive comparative analysis, we evaluate the statistical and morphological properties, including the two-point correlation function, and distribution of pore characteristics such as volume, area, and orientation, as well as permeability.

2.1 Sample Material, Image Acquisition & Processing

Berea sandstone, hailing from the Berea Quarry in Ohio (USA), is a well-studied and widely accepted standard reservoir material used by the petroleum industry for many years in laboratory flow experiments (eg., core flooding), flow models, and core analysis research (Pepper et al., 1954; Hazlett, 1995; Øren & Bakke, 2003; Bera et al., 2011; S. Berg et al., 2014; Leu et al., 2014; Sharqawy, 2016). The Berea sandstone is chosen for its accessibility, cost-effectiveness, and well-studied nature, which enables comparison of our results with those of previous studies. The porosity and permeability typically measured ranges from approximately 12% to 26% and from $2{\times}10^{-13}$ to $2{\times}10^{-12}$ m^2 respectively (Churcher et al., 1991; Mostaghimi et al., 2013; Peng et al., 2014; Soulaine et al., 2016; Mosser et al., 2017).

2.1.1 X-ray Microtomography

A 3D volume, used for ground truthing, was obtained from an 8mm drill-core of Berea sandstone, imaged using a Zeiss Xradia 610 Versa high-resolution 3D X-ray μCT with a $0.4\times$ objective lens, 70.0kV accelerating voltage, and 123μA current. A low-energy filter (LE4) was used to increase the average beam energy and subsequently improve the transmission of X-rays through the sample. A pixel size of 11.41 μm ($11.4 \times 11.4 \times 11.4$ μm voxels^3) is determined by the objective lens strength and relative position of the source, sample, and detector. In total, 2,001 radiograph projections of size 1024 by 1024 pixels (11.67 mm by 11.67 mm) were digitized and represented by an array of greyscale values reflecting differences in absorption contrast.

2.1.2 SEM Images

The first set of 2D images consists of three orthogonal thin sections imaged in backscattered electron (BSE) mode using the Atlas software installed on a Zeiss Gemini 450 SEM which allows for automated large-area imaging of up to several centimeters. During acquisition, a beam intensity of 10kV, probe current of 1.0nA, and pixel size of 3.8 μm was used resulting in three large grayscale BSE images of dimensions 2048 by 2048 pixels (7.78 mm by 7.78 mm), 2048 by 3584 pixels (7.78 mm by 13.62 mm), and 4096 by 4096 pixels (15.56 mm by 15.56 mm) for the x, y, and z directions, respectively. These images are herein referred to as BSE images.

2.1.3 Optical Images

For the second set of 2D images a drill core, impregnated with blue epoxy to highlight the pore spaces and aid in the segmentation process, was cut into three orthogonal sections. The sections were imaged with a Zeiss Axioscan 7 Microscope Slide Scanner, an optical polarizing light microscope combined with high-speed slide digitization capabilities. Each section was scanned in full color (3 channels: RGB) under plane-polarized light (PPL) at $10\times$ magnification with a pixel size of 0.44μm producing three large images of dimensions 50704 by 32005 pixels (22.23 mm by 14.04 mm), 50573 by 27240 pixels (22.20 mm by 11.95 mm), and 41164 by 41164 pixels (18.05 mm by 18.049 mm) for the x, y, and z directions respectively.

2.2 Image Processing

To remove noise and artifacts common in raw images, the acquired grayscale μCT projections and BSE maps underwent the application of edge-preserving denoising algorithms: the anisotropic diffusion filter (Perona et al., 1994) for μCT projections and the bilateral filter (Tomasi & Manduchi, 1998) for BSE maps. These edge-preserving denoising algorithms promote smoothing within a desired region, facilitating high-resolution edge detection while ensuring the preservation of original object boundaries.

Subsequently, all three datasets—referred to herein as μCT, BSE, and optical images—were segmented into binary images. In these images, the phase of interest, namely pore space, was depicted in white with a pixel value of 1, while non-pores appeared in black with a pixel value of 0. Segmentation was conducted using the pixel-classification workflow in ilastik, a free and open-source interactive image processing toolkit utilized for supervised ML random forest-based image analysis (S. Berg et al., 2019; Sommer et al., 2011).

2.3 Representative Elementary Size (RES) Analysis

Essential to the reconstruction of heterogeneous and complex microstructures is the determination of a representative image size (RES) that captures the structural elements of the system under consideration. Larger training images pose higher computational demands, while overly small images fail to fully capture material behavior and heterogeneity, resulting in the generation of pore artifacts and unrealistic shapes (Amiri et al., 2023). Hence, a RES analysis should be conducted for heterogeneous and complex samples to best determine an appropriate image size for training the model (Volkhonskiy et al., 2019; Costanza-Robinson et al., 2011).

RES analysis is a method used to determine the smallest size of an image that is large enough to effectively capture the whole system's heterogeneity (Bargmann et al., 2018; Gusev, 1997). This is based on the concept of a representative elementary volume (REV), defined as the minimum volume of a material whose effective behavior is representative of that of the material as a whole (Bear & Braester, 1972; Bear, 2013; Aboudi et al., 2013). Typically, RES analysis is applied to individual rock properties, for instance, porosity or permeability (e.g., Mosser et al. (2017)), and serves in the upscaling process to assess macro-scale properties determined from a smaller yet representative sample. However, a RES obtained in this manner can vary significantly based on the specific property under consideration. The methodology involves plotting sample size against the corresponding calculated property and it is commonly observed that the property exhibits significant fluctuations at small sizes but becomes size-insensitive at a certain point, indicating the representative size and marking the transition from micro- to macro-scale (Al-Raoush & Papadopoulos, 2010).

To determine the RES of our sample, we adopted the approach employed by Amiri et al. (2023) which relies on the widely popular two-point correlation function, $S_2(r)$ (Torquato & Haslach Jr, 2002; Jiao et al., 2007, 2008), defined as the probability, P, that two randomly selected points with a distance, r, fall within the same phase of interest (i), V_i, in a d-dimensional space, R^d (Yeong & Torquato, 1998):

$$S_2^{(i)}(r) = P(x \in V_i \ , x + r \in V_i) \text{ for } x \textit{ and } V_i \in R^d \tag{1}$$

where x is an index of pixel locations within the image. This radial form of two-point correlation is calculated by averaging the probabilities in the x, y, and z axes. According to this definition, at $r = 0$, S_2 gives its maximum value, equal to the phase fraction, ϕ, because the definition reduces to the probability of one random point being within the same phase. Then, with increasing the distance, the probability decreases exponentially, ultimately reaching its asymptotic value of ϕ^2 (Jiao et al., 2007).

This method utilizes the two-point correlation function to enable a multifaceted analysis of the pore space within the sample. It goes beyond mere porosity quantification (as denoted by $S_2(r = 0)$) by also encompassing the average pore size. More crucially, it examines the long-range correlations between pores, offering a deeper insight into the spatial distribution and interaction within the pore network. This comprehensive approach integrates both the structural and morphological characteristics of the pore space, culminating in an enriched RES analysis. Such a detailed evaluation is crucial for various post-reconstruction tasks, including fluid flow simulation, where an accurate understanding of the pore structure is essential. However, a scaled version of S_2, known as scaled autocovariance, is used here for RES analysis. This function is calculated as follows:

$$F_2(r) = \frac{S_2(r) - \phi^2}{\phi - \phi^2} \tag{2}$$

where ϕ is the phase fraction (aka porosity). Note that, due to the asymptotic behavior of the two-point correlation function, $F_2(r = 0) = 1$ and $F_2(r \to \infty) = 0$. Using the scaled function is a more convenient method for comparing the spatial correlation of pores across images of varying sizes. This is because after this scaling, at a given distance, a zero value indicates no correlation, whereas positive and negative values mean positive correlation and anticorrelation, respectively.

Here, we calculate the average F_2 curve from 50 random subvolumes of the entire μCT volume. We then compare these curves with that of the whole μCT volume. In particular, we compute the mean square error (MSE) between the F_2 function of the entire image with those of subvolumes within their overlapping ranges. The underlying rationale is that as the size of the image increases, the correlation function of microstructures tends to increasingly resemble that of the whole volume. We identify the REV as the point beyond which further increases in image size result in only negligible reductions in MSE. Subsequently, the calculated REV in the μCT data is utilized to determine the representative image size (i.e., RES) for BSE and optical images, taking into account their respective pixel sizes.

2.4 SliceGAN

First introduced by I. J. Goodfellow et al. (2014), GANs have emerged as a cornerstone in the field of deep generative modeling, revolutionizing various aspects of machine learning, particularly in image processing. GANs have been instrumental in the development of numerous advanced applications, including image-to-image translation (Isola et al., 2017), super-resolution enhancement (Ledig et al., 2017), text-to-image conversion (H. Zhang et al., 2017), semantic image editing (Shen et al., 2020), among others.

The central concept of GANs lies in pitting two players, typically convolutional neural networks (CNNs), against each other in an adversarial setup. One player, known as generator G, is tasked with creating new data that mimics the real data. On the other side, there is a discriminator D which functions as a classifier with the role of distinguishing real images from the generated ones. During the training, the generator learns to produce increasingly realistic fake images, $G(z)$ by mapping a random noise vector z, sampled from Gaussian distribution, to match the distribution of the training data. However, G is not exposed to the real images x; its learning is solely guided by the feedback received from the D's predictions on fake images i.e., $D(G(z))$. Training GANs is fundamentally about achieving a Nash equilibrium within a minimax optimization problem. This process culminates at a saddle point, which represents a minimum with respect to the generator G and a maximum with respect to the discriminator D. Ideally, at this equilibrium, G should be adept enough to 'fool' D by generating images so realistic that D misclassifies them as real (I. J. Goodfellow et al., 2014; I. Goodfellow, 2016). Despite their remarkable capability in image generation and a wide array of applications, GANs encounter several technical challenges. These include training instability, mode collapse, non-convergence, and diminished gradient. These challenges have spurred a significant amount of research aimed at addressing these issues, resulting in the development of numerous GAN variants. Each of these variants is tailored to enhance the training process or to modify the architecture for specific applications. For a comprehensive overview of these topics, the reader is referred to the reviews by Gui et al. (2023) and Ferreira et al. (2022).

SliceGAN is one of these variants utilizing Wasserstein loss with gradient penalty (WGAN-GP) (Gulrajani et al., 2017) to stabilize the training and mitigate the issue of mode collapse. In the context of reconstructing 3D images from 2D slices, SliceGAN employs a unique architecture comprising a 3D generator with 3D transpose convolution layers, alongside three 2D discriminators, each consisting of 2D convolutional layers and corresponding to a specific plane. During training, the generator creates 3D images. Random slices from these generated images, representing different planes, are then fed into the respective discriminators. The real inputs for the discriminators, however, are derived from a real 3D image. These are randomly sliced along the same planes as those used for the generated images. This approach, while innovative, still necessitates reliance on real 3D inputs for training.

In this study, we modify the training process so that real 2D images to the discriminator are randomly extracted from large BSE and optical images acquired from different planes of the sample, as described before. Furthermore, to evaluate the generator's performance, we compute the MSE between the two-point correlation function for generated volumes and those of 2D images across different orientations during training. This microstructure-based metric serves as a computationally efficient and interpretable tool for assessing the efficacy of the generator in capturing the structural and morphological information in the 2D images. Additionally, we have made alterations to the network architecture of both the generator and discriminator to accommodate larger training images and to decrease the checkerboard artifacts in the generated volumes.

Figure 1 illustrates the modified workflow implemented in this study. After the preparation of thin sections, we acquire large-area BSE and optical images, which are then segmented into pore and solid phases. Subsequently, we extract random crops with RES size from these 2D images, taken from different orientations. Since we use different imaging techniques with varying pixel sizes, calculating RES for each is a crucial step in ensuring that input data for our SliceGAN reflects the pore space characteristics of the Berea sandstone. These crops are then resized on-the-fly to 256^2 pixels using the Lancsoz filter and supplied to the corresponding discriminator throughout the training process. This size represents the maximum capacity feasible within our GPU memory constraints. Each discriminator, D_i, also receives slices from the corresponding plane of generated volumes, $G(z)_i$. Finally, the loss functions for D and G are calculated as :

$$L_{D_i} = -\mathbb{E}_{x\sim p(data)}(D_i(x_i)) + \mathbb{E}_{z\sim p(z)} D_i(G(z)_i) + \lambda \mathbb{E}_{\hat{x}_i}[(\left\|\nabla_{\hat{x}_i} D(\hat{x}_i)\right\|_2 - 1)^2] \tag{3}$$

$$L_G = \sum_{i=1}^{3} -\mathbb{E}_{z\sim p(z)} D_i(G(z)_i) \tag{4}$$

where i = 1,2,3 corresponds to x, y, z planes, respectively. The coefficient λ controls the degree of penalization on the gradients of D, and $\hat{x}_i$ represents a mixture of real and the generated slices in each plane. From Equation 4, it is apparent that no information about the real images, x_i, is used for training the generator. Instead, it learns from feedback from the discriminators on the different planes i.e., $D_i(G(z)_i)$.

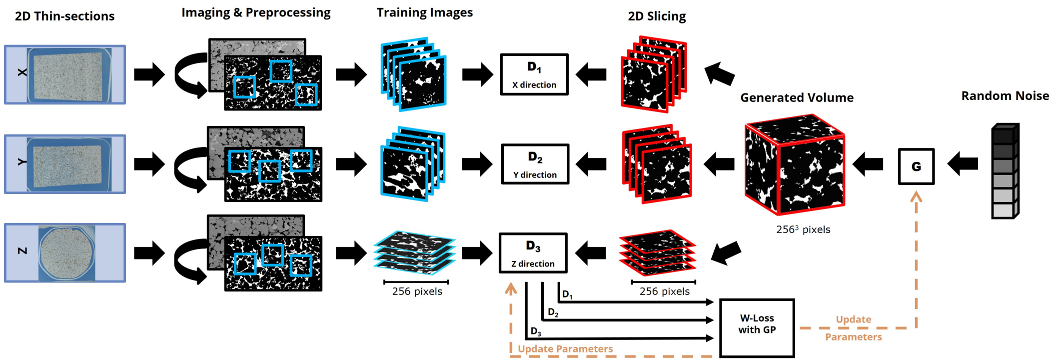

Figure 1. Our modified SliceGAN training workflow for BSE images. A similar workflow is used for optical images. See the text for a detailed explanation.

3 Results

In this section, we assess the performance of our adapted SliceGAN model. Two separate models are trained following the identical workflow outlined in Figure 1: one using BSE images, and the other using optical images. To compare the results of reconstructions with real μCT image, we generate 100 three-dimensional images using the trained SliceGAN model for each BSE and optical data. These synthetic images are then compared to an equivalent number of random subvolumes with REV size from the whole μCT volume. Our comparative analysis employs various metrics, ranging from the distribution of pore characteristics to two-point correlation functions and permeability estimates.

3.1 RES Analysis

Figure 2a presents the results of the REV analysis performed on the entire μCT image, with each curve representing the average F_2 calculated from 50 random subvolumes of specific sizes. These curves are characterized by sharp initial declines followed by a bump at $r \approx 20$, which is approximately equal to the average pore size. Subsequently, most curves exhibit damped oscillations over relatively small ranges, indicating positive correlations between clusters of pores beyond the average pore size. However, the F_2 curves for subvolume sizes 32 and 64 reveal that these sizes are not sufficiently large to capture the average pore size and the interaction between clusters of pores, respectively.

Figure 2b illustrates the normalized mean squared error (MSE) between each curve with that of the whole sample (denoted by the black curve in Figure 2a) within their overlapping ranges. The MSE values have been normalized by the maximum distance (r) for each size. This normalization is important for ensuring that the MSE values are comparable across different sizes, as larger images inherently have more pixels over which errors can accumulate. The graph reveals that the MSE curve levels off at an image size of 128^3 voxels, signifying that further increases in size do not correspond to a notable decrease in MSE.

Based on the interpretation of F_2 curves and MSE analysis, the REV for the μCT data is determined to be 128^3 voxels. This corresponds to a cubic volume with a linear length of 1459.2 μm, calculated as 128×11.4 μm. Using this REV as a benchmark, and considering the pixel sizes for BSE (3.8 μm) and optical images (0.44 μm), we calculate the RESs to be 384^2 pixels for the BSE images and 3324^2 pixels for the optical images. While we utilized a μCT image here, the same approach and interpretation can

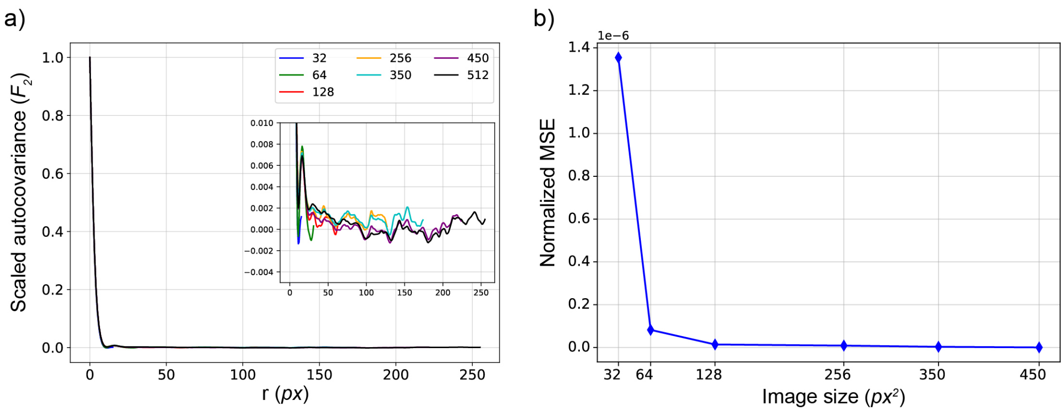

Figure 2. Representative Elementary Volume (REV) analysis on μCT data. a) The average F_2 curves for 50 random subvolumes extracted from our original μCT volume (black curve). The inset of the plot offers a magnified view of the curves at small correlations, b) the normalized MSE calculated between the average F_2 curve of the original image and smaller ones.

be applied to 2D images from various planes to determine the RES when a 3D volume is not available.

However, as previously noted, the training images at the determined RES sizes were downscaled to 256^2 pixels, resulting in a uniform pixel size of 5.7 μm for both BSE and optical imaging modalities. Additionally, all random subvolumes with the size of REV (128^3) were upscaled to 256^3 using trilinear interpolation. Such standardization ensured that the original and reconstructed 3D images shared identical dimensions and voxel sizes, thereby allowing for direct and consistent comparison.

3.2 3D Reconstructions from 2D Images of Porous Media

Two SliceGANs were trained using three orthogonal BSE and optical images. Training time for each model was approximately 24 hours on an NVIDIA RTX A6000 GPU with 48GB memory. This duration included the time taken to evaluate the generator. Our approach for evaluation was to calculate the average S_2 for 100 random images from the large training images in each x, y, and z planes before the training. This average value served as a target S_2 for evaluating the generator performance. During the training, we calculated the average radial 3D S_2 derived from generated images. A mean square error of $1{\times}10^{-5}$ between these two correlation functions was used as a criterion to save the best model.

During the inference phase, we generated one hundred 3D images for both BSE and optical images. Subsequently, these 3D reconstructions underwent a post-processing step, where we applied a morphological closing operation. This operation was performed using a spherical structuring element with a radius of 3 pixels. The closing operation is essentially a two-step process: initially, it dilates the image, and then it is followed by an erosion step. This sequence effectively removes small isolated pores and fills in small holes within the pores.

3.2.1 Visual & Statiscial Analysis

Figure 3 illustrates a random subvolume of μCT data and examples of 3D reconstructions from BSE and optical images, as well as 2D slices across orthogonal orientations. All displayed 3D images are of the same dimensions of 256^3 voxels with the same

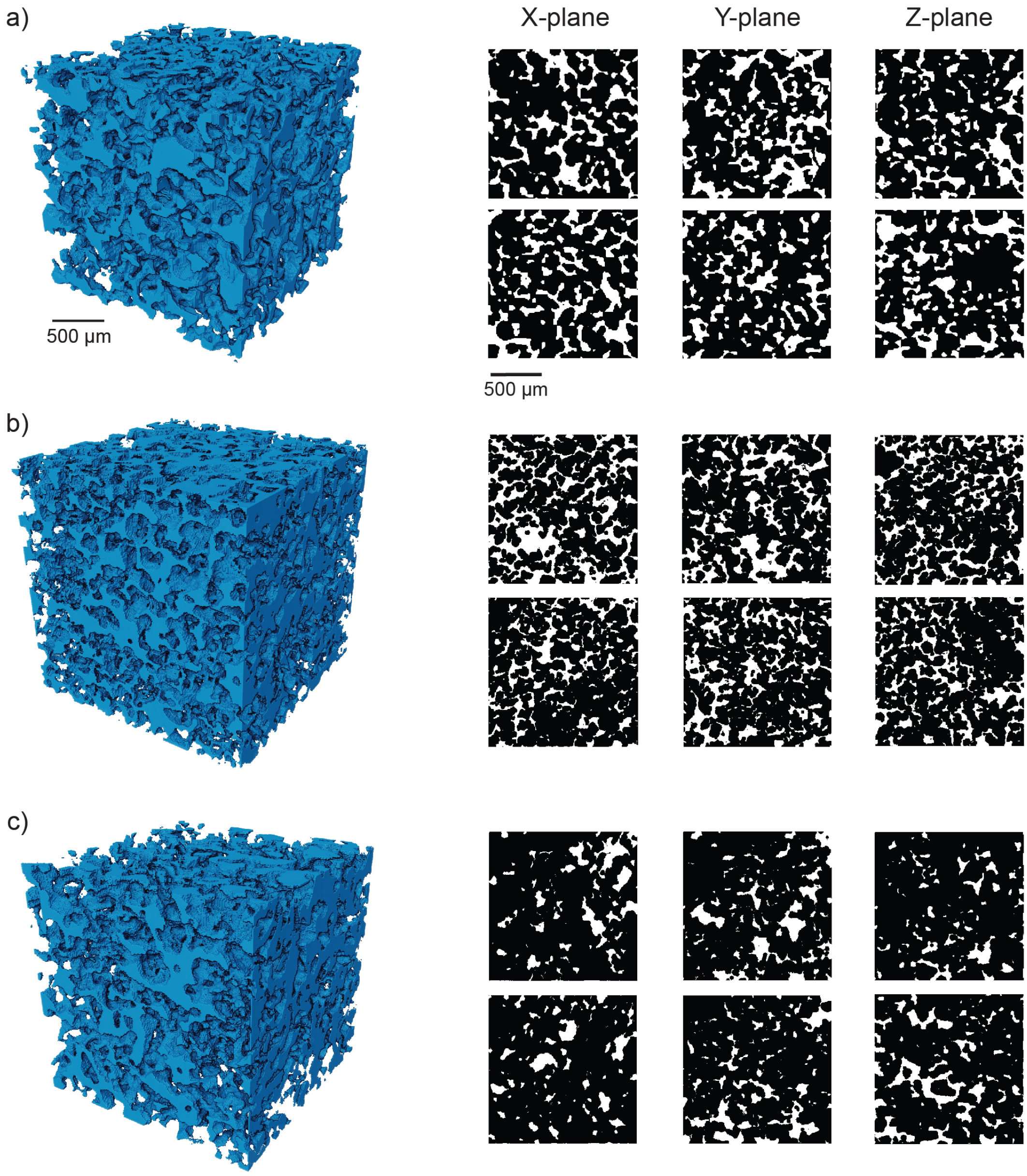

Figure 3. Visual comparison of original μCT (a) with 3D reconstructions from BSE (b) and optical images (c), along with two slices in x, y, and z-planes.

voxel size of 5.7μm, as mentioned previously. It can be seen that the reconstructed 3D images from BSE and optical images exhibit a general resemblance to the original μCT image in terms of structure and spatial distribution of pores. Nevertheless, a closer inspection of 2D slices reveals distinct differences in porosity and pore sizes within the optical image reconstructions when compared to those from BSE and original μCT data.

In addition to visual comparison, three-dimensional S_2 was calculated for the hundred images of μCT subvolumes and 3D-reconstructed images of BSE and optical images. Figure 4 presents the curves for each imaging technique, with solid lines indicating the average values and shaded regions representing the range of the S_2 curves. What stands out in this figure is the close agreement between the average curve of the orig-

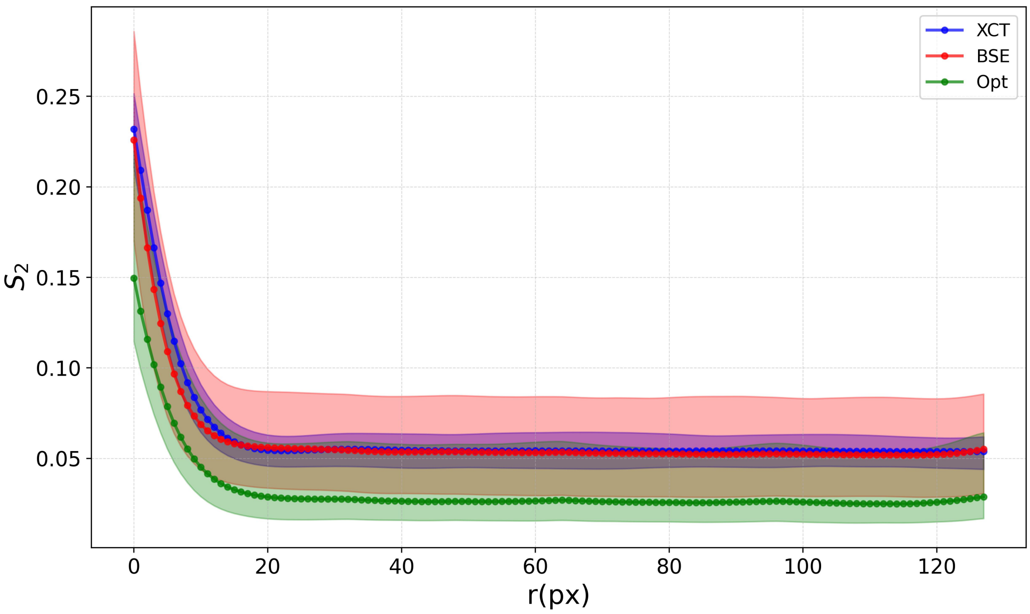

Figure 4. Comparison of the three-dimensional S_2 curves. The solid lines show average values for the original μCT (blue) and generated BSE (red) and optical (green) images. The shaded color surrounding the average curves indicates the variability within each data.

inal μCT and BSE-reconstructed volumes at all ranges. Specifically, the average porosity (i.e., the probability at $r = 0$) is 0.232 for μCT and 0.226 for BSE-reconstructed volumes. Nevertheless, a slightly higher probability is observed in the average curve of μCT images at short ranges (i.e., at $r < 20$ pixels), indicating larger pores on the whole. However, the average S_2 curve obtained from optical images shows a lower average porosity of 0.15. Despite this difference, the general trend is similar to μCT and BSE images, indicating similar spatial distribution of pores in three dimensions.

Figure 5 presents the probability distributions of pore area, volume, and orientation in the original and reconstructed images, calculated using the label analysis tool in Thermo Fisher Scientific AVIZO software (2020 – version 3.1). The results are reported as probability densities in which each bin's height will be the count divided by the total number of observations (i.e., pores) times the bin width. This normalization enables a straightforward comparison of the distributions without being skewed by the number of pores. Overall, the results indicate a similar trend in the distributions of original and reconstructed volumes. Figure 5a-b indicates a power law distribution of pores' surface area and volume towards small values for all images. However, the μCT volumes tend to have greater numbers of large pores than BSE and optical images in which the majority of pores are small.

Figure5d-c compares the distributions of the orientation of the major axis of pores represented by θ and ϕ. The orientation θ, known as azimuth angle, is the angle in the xy-plane counted in the positive direction from the x-axis and ranges from $-180°$ to $+180°$. The orientation ϕ is the altitude angle measured from the positive z-axis (vertical axes in Figure3) and ranges from $0°$ to $90°$. From these distributions, we can see that the majority of the pores in all images exhibit a concentration around an altitude angle of $90°$ (Figure5c), and azimuth angles of $0°$ and $100°$ (Figure5d). However, 3D reconstructions from BSE and optical images show a larger number of pores oriented around azimuth of $0°$ and altitude angle of $90°$ than pores in μCT images.

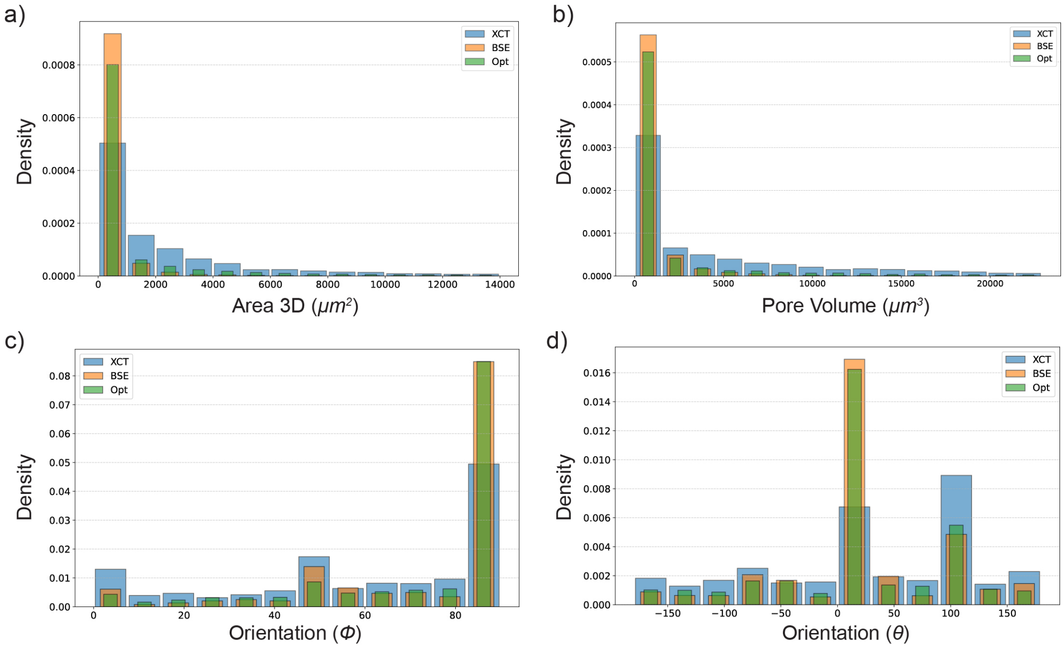

Figure 5. Distributions of pore characteristics a) area, b) pore size distribution (pore volume), c) altitude angle (ϕ), and d) azimuth angle (θ) for optical (Opt), backscattered (BSE), and X-ray tomography (XCT) images.

3.2.2 Permeability

To further assess the accuracy of the reconstructed pore microstructures and their impact on macroscopic transport properties, we estimated the effective permeability of the original μCT images and the reconstructions using a voxel-based Finite Element Method (FEM) introduced by P. C. Lopes et al. (2023). In particular, the GPU implementation of this method (P. C. F. Lopes et al., 2022) allows for efficient permeability computation of hundreds of volumes for each set of μCT images, as well as reconstructions from BSE and optical images. Figure6 illustrates a box plot comparing the permeability values averaged along the x, y, and z axes. The plot reveals that the μCT images hold the highest average permeability, followed by BSE reconstructions, while optical images maintain the lowest. Additionally, the μCT volumes demonstrate less variability, as evidenced by the shorter 'whiskers' on the box plots, compared to the reconstructions. This reduced variability in the μCT volumes is consistent with expectations, considering that the permeability estimates are derived from REVs.

4 Discussion

The primary objective of our research is to assess the accuracy and feasibility of generating authentic 3D digital reconstructions of porous media samples using only 2D images. While numerous studies have explored the realm of 2D-to-3D reconstructions, our review of the literature indicates that these investigations typically utilize 3D ground-truth volumes for training their models. This inherently incorporates the three-dimensional spatial characteristics of the pore space into the models. In contrast, our methodology relies solely on large 2D images in different orientations from which representative images are sampled and used for training. To capture these images, we employed two distinct imaging techniques: BSE with a pixel size of 3.8 μm, and optical microscopy with

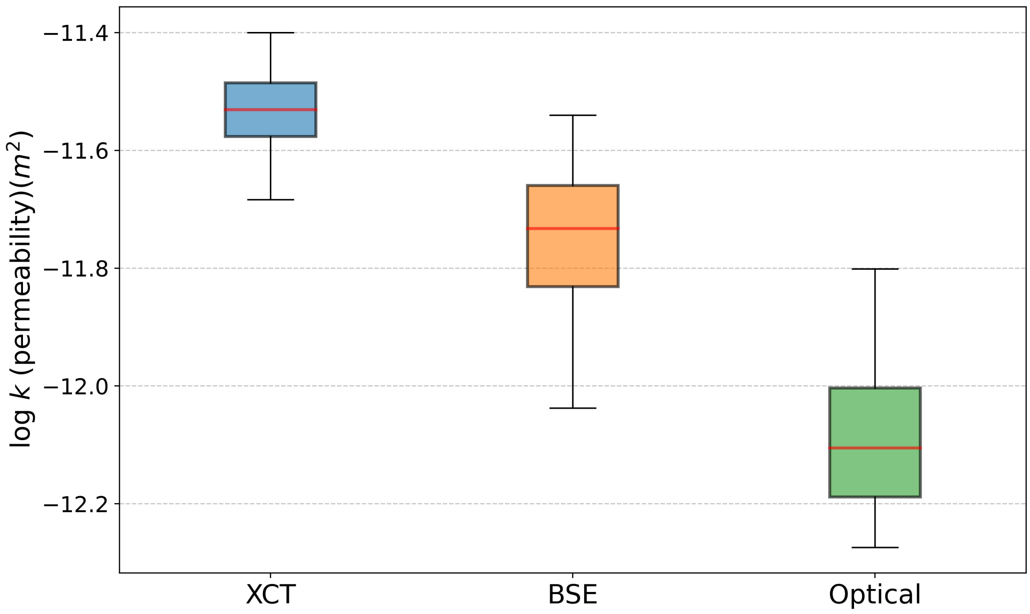

Figure 6. The statistical analysis of permeability estimates derived from subvolumes of REV size of the original μCT, and reconstructed BSE and optical volumes.

a pixel size of 0.44 μm. This dual-modality approach allows for a detailed and varied representation of the sandstone's microstructure across scales.

In general, our findings show that high-fidelity 3D microstructures with similar morphological and transport properties to those of original 3D images can be reconstructed from only 2D images. In particular, a close agreement is found between BSE-reconstructed and real μCT volumes in terms of different metrics. However, from Figure5a-b, it can be seen that the BSE-reconstructed volumes possess smaller pores than the μCT data. This can be explained by the higher resolution of BSE images which allows for detecting smaller pores in 2D images which have been subsequently reproduced in 3D reconstructions. These finer pores, which can be similarly seen in the results of optical images, typically tend to have spherical shapes whose estimated major axes using inertia moments are likely to be in the xy-plane with a ϕ close to 90°, as shown in Figure5c.

The average S_2 curves, as depicted by solid lines in Figure4, demonstrate a notable alignment between BSE and μCT images across both short and long ranges. Interestingly, our findings indicate that the BSE images cover a wider range of values than those of the μCT images. For instance, the porosity derived from BSE images ranges from 0.17 to 0.29 while this range is between 0.21 and 0.25 for the μCT subvolumes. This diversity in the generated images is an important attribute of our model, which can be partially attributed to the loss function employed. Specifically, the use of Wasserstein loss, combined with the gradient penalty, helps to prevent mode collapse, thereby encouraging diversity. Another contributing factor to this diversity could be the large sizes of original 2D images, scanned from three distinct planes of the sample. This latter point will be elaborated upon in greater detail later in the text. On the other hand, the low variability in μCT images, illustrated by the narrower shaded blue region, aligns with the expectations, as the subvolumes are of REV size. Consequently, the properties within these subvolumes are expected to exhibit minimal variation.

Similarly, the model trained with optical images has successfully reconstructed a diverse array of images, as evidenced by the broad green shading in Figure 4. Despite this diversity, a noticeable discrepancy is observed between the optical reconstructions and the other modalities, characterized by consistently lower probabilities across all ranges. This divergence can be explained by lower porosity in the large optical images used for training, ranging from 0.08 to 0.15 across different planes. This contradicts the expectation of higher porosity detection at greater image resolutions. The segmentation challenges of RGB optical images, even with blue epoxy impregnation, may contribute to this discrepancy. Difficulties in distinguishing pore spaces from grain boundaries during manual labeling of optical images have likely resulted in an underestimation of pores by our ML-based segmentation tool.

The statistical analysis of permeability, as illustrated in Figure6, also indicates a higher variability in permeability of the BSE and optical than μCT images. Despite this variability, the median permeability value of μCT images remains higher than that of BSE reconstructions, which in turn is higher than the permeability of optical images. Consistent with previous results, this suggests that the increased porosity in some of the BSE-reconstructed images is due to the detection of the smaller pores in higher-resolution images that do not typically enhance the flow path and therefore permeability. Compared to the permeability results from BSE and μCT images, which are in the same order of magnitude, the optical reconstructions exhibit the lowest values. This difference can be attributed to a 7 percent reduction in average porosity obtained from the optical reconstructions relative to the other modalities, as shown in Figure4.

Figure7 compares our porosity and permeability estimates with those from prior research on Berea sandstone, specifically focusing on studies using X-ray tomography to investigate the impact of voxel and sample sizes on permeability. Our results indicate that the estimates derived from our BSE and optical reconstructions align closely with previous studies for both porosity and permeability. In contrast, the permeability appears to be slightly overestimated in our μCT images, likely due to the lower resolution (11.4 μm in the original μCT volume) in our study. Such a resolution can cause an overestimation of pore sizes due to the partial volume effect (PVE), as discussed by Wildenschild and Sheppard (2013), posing challenges in accurate pore identification. The marker sizes in this plot represent the relative linear length of the samples analyzed, as reported in Table 1. In the case of Mosser et al. (2017), this linear length, calculated as the edge-length multiplied by voxel size, is 1.2 mm for the whole sample (the larger orange marker) and 0.192 mm for REVs which is too small to be representative. Therefore, this discrepancy can be attributed to the non-representative samples used in this study.

A prominent finding of our study is the great variability observed in the reconstructed volumes. This is important as the limited generalization is a major challenge of GANs (and generative models in general) where models struggle to extrapolate to unseen data. This aspect is particularly crucial in studying heterogeneous rocks whose properties can vary significantly from one sample to another. Our results demonstrate the model's ability to generate not only realistic but also diverse 3D microstructures from 2D images. A key factor underpinning this diversity, as previously discussed, is the utilization of large 2D images from which training images are randomly sampled during the training. This enables the model to encompass a wider array of variations within the sample, effectively capturing the intricate details and heterogeneity present. For example, the linear length for our entire μCT image, calculated as the edge-length multiplied by the voxel size (i.e., $512\times 11.4\mu$m), is 5.84 mm, while for the REV volumes, it stands at 1.46 mm. In contrast, the linear lengths of the large 2D images obtained from different planes range from 7.78 mm to 15.56 mm for BSE images and between 11.95 mm and 23 mm for optical images.

In summary, our findings are significant in two major respects. First, our results show that we can use only 2D images to reconstruct realistic 3D microstructures with

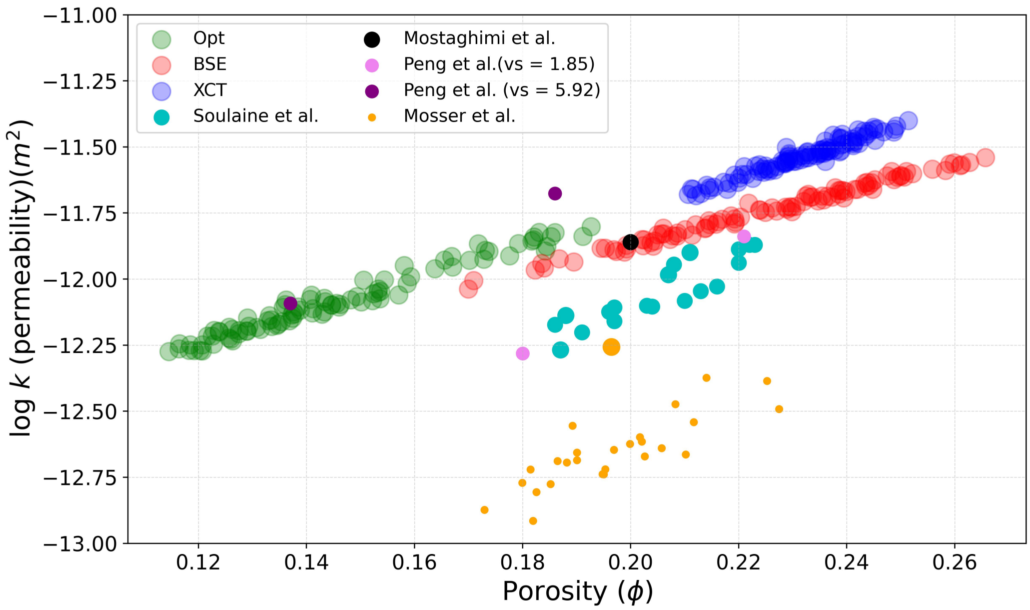

Figure 7. Comparison of our estimation of porosity and permeability with previous studies on Berea sandstone. The VS in the legend stands for the voxel size used in the study.

similar characteristics to real ones. This is crucial in cases where the maximum resolution of common X-ray tomography machines ($\approx 500nm$) is insufficient to capture the finer features within the sample. Second, the great variation in our 3D reconstructed images, i,e., the range of estimated porosity and permeability, is particularly promising as our results closely match the values reported in previous studies. In essence, our results indicate that instead of performing several X-ray tomographies, it is possible to generate diverse 3D images from sufficiently large 2D images. This notable diversity in reconstruction offers a critical advantage, facilitating comprehensive assessments of variability and uncertainty in various sample properties. Such evaluations are particularly crucial for anisotropic and heterogeneous rocks, where quantifying these variations is integral to accurately characterizing the sample.

Table 1. Comparison of sample size and the voxel size of our study with previous research on Berea sandstone. For our μCT images, the values in the parentheses are from the whole μCT image. For BSE and optical images, these values report the pixel size and the linear length of the original 2D images scanned.

Reference	Voxel size (μm)	Volume (mm^3)	Linear length (mm)
Our μCT	5.7 (11.4)	3.11 (199)	1.46 (5.84)
Our BSE	5.7 (3.80)	3.11	1.46 (7.78 -15.56)
Our optical	5.7 (0.439)	3.11	1.46 (11.95 -23)
Soulaine et al. (2016)	3.16	0.85 , 1.35	0.95, 1.11
Mostaghimi et al. (2013)	5.3	0.5	0.8
Peng et al. (2014)	1.85, 5.92	0.31	0.68
Mosser et al. (2017)	3	0.007, 1.73	0.192, 1.2

5 Conclusion

This study embarked on an exploration of the potential to accurately reconstruct 3D porous structures using pure 2D electron (SEM) and optical microscopy images at three orientations. Our findings show that when trained well with representative 2D images, our adapted SliceGAN can generate 3D microstructures that closely emulate real ones in terms of structural, morphological, and transport properties. Berea sandstone served as an ideal benchmark, enabling direct comparison with actual 3D images and previous works. However, the most compelling application of our 2D-to-3D reconstruction approach is in analyzing rocks where the features of interest are finer than the maximum resolution achievable with common μCT imaging, and display a level of heterogeneity and variability that cannot be captured by the limited field of view of, e.g., focused ion beam (FIB)-SEM tomography. In such scenarios, our approach can sidestep 3D imaging constraints, harnessing the extensive coverage and high resolution of SEM and optical imaging techniques. These modalities, with their broad FOV in varying orientations, provide a comprehensive assessment of property variability offering a reliable time- and resource-efficient means of generating diverse yet statistically equivalent 3D volumes from readily available 2D images.

6 Open Research

The original segmented BSE, optical, and micro-CT images as well as the data to reproduce the figures are freely available at Utrecht University Yoda data repository: `https://public.yoda.uu.nl/geo/UU01/DO6LT4.html`. Python scripts are also accessible via `https://github.com/hamediut/True2Dto3Drecon`.

Acknowledgments

This research was supported by a European Research Council (ERC) starting grant "nanoEARTH" (852069) in addition to a NWO DeepNL Grant (DeepNL.2018.044). We additionally acknowledge the Utrecht University Electron Microscopy Facility and would like to thank our friends and colleagues within the Department of Earth Sciences for their support.

References

Aboudi, J., Arnold, S. M., & Bednarcyk, B. A. (2013). *Micromechanics of composite materials: a generalized multiscale analysis approach.* Butterworth-Heinemann.

Al-Raoush, R., & Papadopoulos, A. (2010). Representative elementary volume analysis of porous media using x-ray computed tomography. *Powder technology*, *200*(1-2), 69–77.

Al-Raoush, R., & Willson, C. S. (2005). A pore-scale investigation of a multiphase porous media system. *Journal of Contaminant Hydrology*, *77*(1-2), 67–89.

Amiri, H., Vasconcelos, I., Jiao, Y., Chen, P.-E., & Plümper, O. (2023). Quantifying microstructures of earth materials using higher-order spatial correlations and deep generative adversarial networks. *Scientific reports*, *13*(1), 1805.

Bakke, S., & Øren, P.-E. (1997). 3-d pore-scale modelling of sandstones and flow simulations in the pore networks. *Spe Journal*, *2*(02), 136–149.

Bargmann, S., Klusemann, B., Markmann, J., Schnabel, J. E., Schneider, K., Soyarslan, C., & Wilmers, J. (2018). Generation of 3d representative volume elements for heterogeneous materials: A review. *Progress in Materials Science*, *96*, 322–384.

Bear, J. (2010). *Modeling groundwater flow and contaminant transport* (Vol. 23). Springer.

Bear, J. (2013). *Dynamics of fluids in porous media.* Courier Corporation.

Bear, J., & Braester, C. (1972). On the flow of two immscible fluids in fractured porous media. In *Developments in soil science* (Vol. 2, pp. 177–202). Elsevier.

Bera, B., Mitra, S. K., & Vick, D. (2011). Understanding the micro structure of berea sandstone by the simultaneous use of micro-computed tomography (micro-ct) and focused ion beam-scanning electron microscopy (fib-sem). *Micron*, *42*(5), 412–418.

Berg, C. F., Lopez, O., & Berland, H. (2017). Industrial applications of digital rock technology. *Journal of Petroleum Science and Engineering*, *157*, 131–147.

Berg, S., Armstrong, R., Ott, H., Georgiadis, A., Klapp, S. A., Schwing, A., ... others (2014). Multiphase flow in porous rock imaged under dynamic flow conditions with fast x-ray computed microtomography. *Petrophysics*, *55*(04), 304–312.

Berg, S., Kutra, D., Kroeger, T., Straehle, C. N., Kausler, B. X., Haubold, C., ... others (2019). Ilastik: interactive machine learning for (bio) image analysis. *Nature methods*, *16*(12), 1226–1232.

Blunt, M. J. (2017). *Multiphase flow in permeable media: A pore-scale perspective.* Cambridge university press.

Blunt, M. J., Bijeljic, B., Dong, H., Gharbi, O., Iglauer, S., Mostaghimi, P., ... Pentland, C. (2013). Pore-scale imaging and modelling. *Advances in Water resources*, *51*, 197–216.

Blunt, M. J., & Lin, Q. (2022). Flow in porous media in the energy transition. *Engineering*, *14*, 10–14.

Bodla, K. K., Garimella, S. V., & Murthy, J. Y. (2014). 3d reconstruction and design of porous media from thin sections. *International Journal of Heat and Mass Transfer*, *73*, 250–264.

Bond-Taylor, S., Leach, A., Long, Y., & Willcocks, C. G. (2021). Deep generative modelling: A comparative review of vaes, gans, normalizing flows, energy-based and autoregressive models. *IEEE transactions on pattern analysis and machine intelligence*.

Bostanabad, R., Zhang, Y., Li, X., Kearney, T., Brinson, L. C., Apley, D. W., ... Chen, W. (2018). Computational microstructure characterization and reconstruction: Review of the state-of-the-art techniques. *Progress in Materials Science*, *95*, 1–41.

Brandon, D., & Kaplan, W. D. (2013). *Microstructural characterization of materials.* John Wiley & Sons.

Chen, P.-E., Xu, W., Chawla, N., Ren, Y., & Jiao, Y. (2019). Hierarchical n-point polytope functions for quantitative representation of complex heterogeneous materials and microstructural evolution. *Acta Materialia*, *179*, 317–327.

Chung, H., & Ye, J. C. (2021). Reusability report: Feature disentanglement in generating a three-dimensional structure from a two-dimensional slice with slicegan. *Nature Machine Intelligence*, *3*(10), 861–863.

Churcher, P., French, P., Shaw, J., & Schramm, L. (1991). Rock properties of berea sandstone, baker dolomite, and indiana limestone. In *Spe international conference on oilfield chemistry?* (pp. SPE–21044).

Cnudde, V., & Boone, M. N. (2013). High-resolution x-ray computed tomography in geosciences: A review of the current technology and applications. *Earth-Science Reviews*, *123*, 1–17.

Costanza-Robinson, M. S., Estabrook, B. D., & Fouhey, D. F. (2011). Representative elementary volume estimation for porosity, moisture saturation, and air-water interfacial areas in unsaturated porous media: Data quality implications. *Water Resources Research*, *47*(7).

Dahari, A., Kench, S., Squires, I., & Cooper, S. J. (2023). Fusion of complementary 2d and 3d mesostructural datasets using generative adversarial networks. *Advanced Energy Materials*, *13*(2), 2202407.

Dehghan Khalili, A., Arns, J.-Y., Hussain, F., Cinar, Y., Pinczewski, W., Arns, C. H., et al. (2013). Permeability upscaling for carbonates from the pore scale by use of multiscale x-ray-ct images. *SPE Reservoir Evaluation & Engineering*, *16*(04), 353–368.

Feng, J., He, X., Teng, Q., Ren, C., Chen, H., & Li, Y. (2019). Reconstruction of porous media from extremely limited information using conditional generative adversarial networks. *Physical Review E*, *100*(3), 033308.

Feng, J., Teng, Q., Li, B., He, X., Chen, H., & Li, Y. (2020). An end-to-end three-dimensional reconstruction framework of porous media from a single two-dimensional image based on deep learning. *Computer Methods in Applied Mechanics and Engineering*, *368*, 113043.

Ferreira, A., Li, J., Pomykala, K. L., Kleesiek, J., Alves, V., & Egger, J. (2022). Gan-based generation of realistic 3d data: A systematic review and taxonomy. *arXiv preprint arXiv:2207.01390*.

Fu, J., Xiao, D., Li, D., Thomas, H. R., & Li, C. (2022). Stochastic reconstruction of 3d microstructures from 2d cross-sectional images using machine learning-based characterization. *Computer Methods in Applied Mechanics and Engineering*, *390*, 114532.

Gayon-Lombardo, A., Mosser, L., Brandon, N. P., & Cooper, S. J. (2020). Pores for thought: generative adversarial networks for stochastic reconstruction of 3d multi-phase electrode microstructures with periodic boundaries. *npj Computational Materials*, *6*(1), 82.

Gommes, C. J., Jiao, Y., & Torquato, S. (2012). Microstructural degeneracy associated with a two-point correlation function and its information content. *Physical Review E*, *85*(5), 051140.

Goodfellow, I. (2016). Nips 2016 tutorial: Generative adversarial networks. *arXiv preprint arXiv:1701.00160*.

Goodfellow, I. J., Pouget-Abadie, J., Mirza, M., Xu, B., Warde-Farley, D., Ozair, S., ... Bengio, Y. (2014). Generative adversarial networks. *arXiv preprint arXiv:1406.2661*.

Guan, K. M., Anderson, T. I., Creux, P., & Kovscek, A. R. (2021). Reconstructing porous media using generative flow networks. *Computers & Geosciences*, *156*, 104905.

Gui, J., Sun, Z., Wen, Y., Tao, D., & Ye, J. (2023). A review on generative adversarial networks: Algorithms, theory, and applications. *IEEE Transactions on Knowledge and Data Engineering*, *35*(4), 3313-3332. doi: 10.1109/TKDE.2021.3130191

Gulrajani, I., Ahmed, F., Arjovsky, M., Dumoulin, V., & Courville, A. C. (2017). Improved training of wasserstein gans. *Advances in neural information processing systems*, *30*.

Gusev, A. A. (1997). Representative volume element size for elastic composites: a numerical study. *Journal of the Mechanics and Physics of Solids*, *45*(9), 1449–1459.

Hajizadeh, A., Safekordi, A., & Farhadpour, F. A. (2011). A multiple-point statistics algorithm for 3d pore space reconstruction from 2d images. *Advances in water Resources*, *34*(10), 1256–1267.

Hazlett, R. (1995). Simulation of capillary-dominated displacements in microtomographic images of reservoir rocks. *Transport in porous media*, *20*, 21–35.

Heinemann, N., Alcalde, J., Miocic, J. M., Hangx, S. J., Kallmeyer, J., Ostertag-Henning, C., ... others (2021). Enabling large-scale hydrogen storage in porous media–the scientific challenges. *Energy & Environmental Science*, *14*(2), 853–864.

Hemes, S., Desbois, G., Urai, J. L., Schröppel, B., & Schwarz, J.-O. (2015). Multi-scale characterization of porosity in boom clay (hades-level, mol, belgium) using a combination of x-ray μ-ct, 2d bib-sem and fib-sem tomography. *Micro-*

porous and mesoporous materials, *208*, 1–20.

Isola, P., Zhu, J.-Y., Zhou, T., & Efros, A. A. (2017). Image-to-image translation with conditional adversarial networks. In *Proceedings of the ieee conference on computer vision and pattern recognition* (pp. 1125–1134).

Jiao, Y., Stillinger, F., & Torquato, S. (2007). Modeling heterogeneous materials via two-point correlation functions: Basic principles. *Physical review E*, *76*(3), 031110.

Jiao, Y., Stillinger, F., & Torquato, S. (2008). Modeling heterogeneous materials via two-point correlation functions. ii. algorithmic details and applications. *Physical Review E*, *77*(3), 031135.

Jiao, Y., Stillinger, F., & Torquato, S. (2010). Geometrical ambiguity of pair statistics: Point configurations. *Physical Review E*, *81*(1), 011105.

Karras, T., Aila, T., Laine, S., & Lehtinen, J. (2017). Progressive growing of gans for improved quality, stability, and variation. *arXiv preprint arXiv:1710.10196*.

Karras, T., Laine, S., & Aila, T. (2019). A style-based generator architecture for generative adversarial networks. In *Proceedings of the ieee/cvf conference on computer vision and pattern recognition* (pp. 4401–4410).

Karsanina, M. V., & Gerke, K. M. (2018). Hierarchical optimization: Fast and robust multiscale stochastic reconstructions with rescaled correlation functions. *Physical review letters*, *121*(26), 265501.

Kench, S., & Cooper, S. J. (2021). Generating three-dimensional structures from a two-dimensional slice with generative adversarial network-based dimensionality expansion. *Nature Machine Intelligence*, *3*(4), 299–305.

Kingma, D. P., & Dhariwal, P. (2018). Glow: Generative flow with invertible 1x1 convolutions. *Advances in neural information processing systems*, *31*.

Kingma, D. P., & Welling, M. (2013). Auto-encoding variational bayes. *arXiv preprint arXiv:1312.6114*.

Krevor, S., Blunt, M. J., Benson, S. M., Pentland, C. H., Reynolds, C., Al-Menhali, A., & Niu, B. (2015). Capillary trapping for geologic carbon dioxide storage–from pore scale physics to field scale implications. *International Journal of Greenhouse Gas Control*, *40*, 221–237.

Laloy, E., Hérault, R., Lee, J., Jacques, D., & Linde, N. (2017). Inversion using a new low-dimensional representation of complex binary geological media based on a deep neural network. *Advances in water resources*, *110*, 387–405.

Ledig, C., Theis, L., Huszár, F., Caballero, J., Cunningham, A., Acosta, A., … others (2017). Photo-realistic single image super-resolution using a generative adversarial network. In *Proceedings of the ieee conference on computer vision and pattern recognition* (pp. 4681–4690).

Leu, L., Berg, S., Enzmann, F., Armstrong, R. T., & Kersten, M. (2014). Fast x-ray micro-tomography of multiphase flow in berea sandstone: A sensitivity study on image processing. *Transport in Porous Media*, *105*(2), 451–469.

Li, J., Teng, Q., Zhang, N., Chen, H., & He, X. (2023). Deep learning method of stochastic reconstruction of three-dimensional digital cores from a two-dimensional image. *Physical Review E*, *107*(5), 055309.

Li, K.-Q., Li, D.-Q., & Liu, Y. (2020). Meso-scale investigations on the effective thermal conductivity of multi-phase materials using the finite element method. *International Journal of Heat and Mass Transfer*, *151*, 119383.

Lichtner, P. C., & Karra, S. (2014). Modeling multiscale-multiphase-multicomponent reactive flows in porous media: Application to co2 sequestration and enhanced geothermal energy using pflotran. *Computational Models for CO2 Geo-sequestration & Compressed Air Energy Storage*, 81–136.

Liu, S., Zhong, Z., Takbiri-Borujeni, A., Kazemi, M., Fu, Q., & Yang, Y. (2019). A case study on homogeneous and heterogeneous reservoir porous media reconstruction by using generative adversarial networks. *Energy Procedia*, *158*, 6164–6169.

Lopes, P. C., Vianna, R. S., Sapucaia, V. W., Semeraro, F., Leiderman, R., & Pereira, A. M. (2023). Simulation toolkit for digital material characterization of large image-based microstructures. *Computational Materials Science*, *219*, 112021.

Lopes, P. C. F., Pereira, A. M. B., Clua, E. W. G., & Leiderman, R. (2022). A gpu implementation of the pcg method for large-scale image-based finite element analysis in heterogeneous periodic media. *Computer Methods in Applied Mechanics and Engineering*, *399*, 115276.

Menke, H., Reynolds, C., Andrew, M., Nunes, J. P., Bijeljic, B., & Blunt, M. (2018). 4d multi-scale imaging of reactive flow in carbonates: Assessing the impact of heterogeneity on dissolution regimes using streamlines at multiple length scales. *Chemical Geology*, *481*, 27–37.

Mirzaee, H., Kamrava, S., & Tahmasebi, P. (2023). Minireview on porous media and microstructure reconstruction using machine learning techniques: Recent advances and outlook. *Energy & Fuels*.

Mosser, L., Dubrule, O., & Blunt, M. J. (2017). Reconstruction of three-dimensional porous media using generative adversarial neural networks. *Physical Review E*, *96*(4), 043309.

Mostaghimi, P., Blunt, M. J., & Bijeljic, B. (2013). Computations of absolute permeability on micro-ct images. *Mathematical Geosciences*, *45*, 103–125.

Øren, P.-E., & Bakke, S. (2003). Reconstruction of berea sandstone and pore-scale modelling of wettability effects. *Journal of petroleum science and engineering*, *39*(3-4), 177–199.

Peng, S., Marone, F., & Dultz, S. (2014). Resolution effect in x-ray microcomputed tomography imaging and small pore's contribution to permeability for a berea sandstone. *Journal of Hydrology*, *510*, 403–411.

Pepper, J. F., de Witt Jr, W., & Demarest, D. F. (1954). Geology of the bedford shale and berea sandstone in the appalachian basin. *Science*, *119*(3094), 512–513.

Perona, P., Shiota, T., & Malik, J. (1994). Anisotropic diffusion. *Geometry-driven diffusion in computer vision*, 73–92.

Sahimi, M. (2011). *Flow and transport in porous media and fractured rock: from classical methods to modern approaches.* John Wiley & Sons.

Sahimi, M., & Tahmasebi, P. (2021). Reconstruction, optimization, and design of heterogeneous materials and media: Basic principles, computational algorithms, and applications. *Physics Reports*, *939*, 1–82.

Sciazko, A., Komatsu, Y., & Shikazono, N. (2021). Unsupervised generative adversarial network for 3-d microstructure synthesis from 2-d image. *ECS Transactions*, *103*(1), 1363.

Shams, R., Masihi, M., Boozarjomehry, R. B., & Blunt, M. J. (2020). Coupled generative adversarial and auto-encoder neural networks to reconstruct three-dimensional multi-scale porous media. *Journal of Petroleum Science and Engineering*, *186*, 106794.

Sharqawy, M. H. (2016). Construction of pore network models for berea and fontainebleau sandstones using non-linear programing and optimization techniques. *Advances in water resources*, *98*, 198–210.

Sheehan, N., & Torquato, S. (2001). Generating microstructures with specified correlation functions. *Journal of Applied Physics*, *89*(1), 53–60.

Shen, Y., Gu, J., Tang, X., & Zhou, B. (2020). Interpreting the latent space of gans for semantic face editing. In *Proceedings of the ieee/cvf conference on computer vision and pattern recognition* (pp. 9243–9252).

Singh, K., Menke, H., Andrew, M., Lin, Q., Rau, C., Blunt, M. J., & Bijeljic, B. (2017). Dynamics of snap-off and pore-filling events during two-phase fluid flow in permeable media. *Scientific reports*, *7*(1), 5192.

Sommer, C., Straehle, C., Koethe, U., & Hamprecht, F. A. (2011). Ilastik: Interactive learning and segmentation toolkit. In *2011 ieee international symposium on biomedical imaging: From nano to macro* (pp. 230–233).

Soulaine, C., Gjetvaj, F., Garing, C., Roman, S., Russian, A., Gouze, P., & Tchelepi, H. A. (2016). The impact of sub-resolution porosity of x-ray microtomography images on the permeability. *Transport in porous media*, *113*, 227–243.

Tahmasebi, P., & Sahimi, M. (2012). Reconstruction of three-dimensional porous media using a single thin section. *Physical Review E*, *85*(6), 066709.

Tang, Y., Hou, C., He, Y., Wang, Y., Chen, Y., & Rui, Z. (2021). Review on pore structure characterization and microscopic flow mechanism of co2 flooding in porous media. *Energy Technology*, *9*(1), 2000787.

Tomasi, C., & Manduchi, R. (1998). Bilateral filtering for gray and color images. In *Sixth international conference on computer vision (ieee cat. no. 98ch36271)* (pp. 839–846).

Torquato, S., & Haslach Jr, H. (2002). Random heterogeneous materials: microstructure and macroscopic properties. *Appl. Mech. Rev.*, *55*(4), B62–B63.

Torquato, S., & Stell, G. (1982). Microstructure of two-phase random media. i. the n-point probability functions. *The Journal of Chemical Physics*, *77*(4), 2071–2077.

Valsecchi, A., Damas, S., Tubilleja, C., & Arechalde, J. (2020). Stochastic reconstruction of 3d porous media from 2d images using generative adversarial networks. *Neurocomputing*, *399*, 227–236.

Volkhonskiy, D., Muravleva, E., Sudakov, O., Orlov, D., Belozerov, B., Burnaev, E., & Koroteev, D. (2019). Reconstruction of 3d porous media from 2d slices. *arXiv preprint arXiv:1901.10233*.

Wildenschild, D., & Sheppard, A. P. (2013). X-ray imaging and analysis techniques for quantifying pore-scale structure and processes in subsurface porous medium systems. *Advances in Water resources*, *51*, 217–246.

Wu, Y., Lin, C., Ren, L., Yan, W., An, S., Chen, B., ... Zhang, Y. (2018). Reconstruction of 3d porous media using multiple-point statistics based on a 3d training image. *Journal of Natural Gas Science and Engineering*, *51*, 129–140.

Wu, Y., Tahmasebi, P., Lin, C., Ren, L., & Dong, C. (2019). Multiscale modeling of shale samples based on low-and high-resolution images. *Marine and Petroleum Geology*, *109*, 9–21.

Wu, Y., Tahmasebi, P., Lin, C., Zahid, M. A., Dong, C., Golab, A. N., & Ren, L. (2019). A comprehensive study on geometric, topological and fractal characterizations of pore systems in low-permeability reservoirs based on sem, micp, nmr, and x-ray ct experiments. *Marine and Petroleum Geology*, *103*, 12–28.

Xia, W., Zhang, Y., Yang, Y., Xue, J.-H., Zhou, B., & Yang, M.-H. (2021). Gan inversion: A survey. *arXiv preprint arXiv:2101.05278*.

Yang, X.-Y., Chen, L.-H., Li, Y., Rooke, J. C., Sanchez, C., & Su, B.-L. (2017). Hierarchically porous materials: synthesis strategies and structure design. *Chemical Society Reviews*, *46*(2), 481–558.

Yang, Y., Liu, F., Yao, J., Iglauer, S., Sajjadi, M., Zhang, K., ... Lisitsa, V. (2022). Multi-scale reconstruction of porous media from low-resolution core images using conditional generative adversarial networks. *Journal of Natural Gas Science and Engineering*, *99*, 104411.

Yeong, C., & Torquato, S. (1998). Reconstructing random media. *Physical review E*, *57*(1), 495.

You, N., Li, Y. E., & Cheng, A. (2021). 3d carbonate digital rock reconstruction using progressive growing gan. *Journal of Geophysical Research: Solid Earth*, *126*(5), e2021JB021687.

Zhang, H., Xu, T., Li, H., Zhang, S., Wang, X., Huang, X., & Metaxas, D. N. (2017). Stackgan: Text to photo-realistic image synthesis with stacked generative adversarial networks. In *Proceedings of the ieee international conference* *on computer vision* (pp. 5907–5915).

Zhang, T., Ni, M., Guan, Q., Li, D., Zhou, S., & Du, Y. (2023). Reconstruction of three-dimensional porous media using multi-scale generative adversarial networks. *Journal of Applied Geophysics*, *213*, 105042.

Zhu, J.-Y., Zhang, R., Pathak, D., Darrell, T., Efros, A. A., Wang, O., & Shechtman, E. (2017). Toward multimodal image-to-image translation. *Advances in neural information processing systems*, *30*.